The temporal evolution of coronal loops observed by GOES-SXI

M. C. López Fuentes^{1,2,*}, J. A. Klimchuk¹, C. H. Mandrini^{2,*}

ABSTRACT

We study the temporal evolution of coronal loops using data from the Solar X-ray Imager (SXI) on board the Geosynchronous Operational Environmental Satellite 12 (GOES-12). This instrument has the advantage of providing continuous soft X-ray observations of the solar corona at a high temporal cadence, which allows us to follow in detail the full lifetime of each of several coronal loops. The observed light curves suggest three somewhat distinct evolutionary phases: rise, main, and decay. The durations and characteristic timescales of these phases [I/(dI/dt)], where I is the loop intensity are much longer than a cooling time and indicate that the loop-averaged heating rate increases slowly, reaches a maintenance level, and then decreases slowly. It does not turn on or off abruptly. This suggests that a single heating mechanism operates for the entire lifetime of the loop. For monolithic (uniform cross section) loops, the loop-averaged heating rate is the intrinsic energy release rate of the heating mechanism. For loops that are bundles of impulsively heated strands, it is an indication of the frequency of occurrence of individual heating events, or nanoflares. We show that the timescale of the loop-averaged heating rate is proportional to the timescale of the observed intensity variation. The constant of proportionality is approximately 1.5 for quasi-steady heating in monolithic loops and 1.0 for impulsive heating in multi-stranded loops. The ratios of the radiative to conductive cooling times in the loops are somewhat less than 1, putting them intermediate between the values measured previously for hotter and cooler loops. The new measurements provide further support for the existence of a trend suggesting that all loops are heated by the same mechanism, or that different mechanisms have fundamental similarities (e.g., are all impulsive or are all steady with similar rates of heating).

Subject headings: Sun: corona – Sun: magnetic fields – Sun: flares – Sun: X-rays

¹Naval Research Laboratory, Code 7675, Washington, DC 20375

²Instituto de Astronomía y Física del Espacio, CONICET-UBA, CC. 67, Suc. 28, 1428 Buenos Aires, Argentina

^{*}Member of the Carrera del Investigador Científico, Consejo Nacional de Investigaciones Científicas y Técnicas, Argentina

1. Introduction

The nature of coronal heating in the Sun and solar-like stars remains one of the most important unexplained problems of Astrophysics. Presently, it is widely accepted that the magnetic field plays a key role in structuring the coronal plasma and providing the energy to achieve the observed coronal temperatures. However, it remains an open question as to how the coronal heating mechanism works. Soft X-ray observations of the Sun show a non-uniform emission coming mostly from the coronal part of active regions (ARs), particularly from so-called coronal loops (Orrall 1981). One therefore expects that the analysis of the temporal evolution of observed loops would provide some clues for solving the coronal heating problem.

In the simplest approach, one can envision loops as monolithic (uniform cross-section) structures in quasi-static equilibrium (see e.g., Rosner et al. 1978). In this picture, a slowly varying heat source nearly balances the energy losses due to thermal conduction and radiation. If the temperature, T, emission measure, EM, loop diameter, d, and loop length, L, are known, one can obtain estimates of the timescales involved in conductive and radiative cooling. A comparison between cooling times and the typical evolutionary timescale for a loop can then be used to test whether the quasi-static interpretation is reasonable. Following this approach, Porter & Klimchuk (1995, henceforth PK95) studied a set of 47 loops observed by the Soft X-ray Telescope (SXT, Tsuneta et al. 1991) on board Yohkoh. In this study they followed individual loops for only a single spacecraft orbit, ~ 1 hr of daylight, and determined evolutionary timescales, I/(dI/dt), where I is the loop intensity. These are "instantaneous" timescales in the sense that the intensity and its derivative are averages over a short time interval, shorter than the timescale itself. Since the computed timescales turned out to be typically one or two orders of magnitude longer than the cooling times, the authors concluded that the loops could be in quasi-static equilibrium. Nevertheless, there remained the question of whether the loops actually persist for as long as their instantaneous evolutionary timescales suggest.

Recent studies based on observations from the Extreme Ultraviolet Imaging Telescope (SoHO/EIT, Delaboudiniere et al. 1995) and the Transition Region and Coronal Explorer (TRACE, Handy et al. 1999) show that most warm loops ($T \sim 10^6$ K) have densities that are not consistent with quasi-static equilibrium (Aschwanden et al. 1999, Aschwanden et al. 2001, Winebarger et al. 2003). One possibility is that coronal loops are bundles of multiple unresolved strands, each of which is independently heated in impulsive events, such as nanoflares (Cargill 1994, Klimchuk 2002, 2006, Warren et al. 2003, Cargill & Klimchuk 2004). This agrees with Parker's conjecture (1988) that energy is released impulsively by reconnection at localized magnetic discontinuities in the corona. These discontinuities are

thought to be formed by the tangling of elemental magnetic ropes via photospheric granular motions. A major goal in coronal physics is to determine whether loops are bundles of strands that are heated by nanoflares or monolithic structures that are heated in a quasi-steady fashion.

Due to the lack of prolonged and continuous observations of individual loops, PK95 were not able to study the lifetimes of loops or how loops evolve during their lifetime (i.e., how the evolutionary timescale changes). In particular, they could not investigate how loops are "born" and how they "die". A complete understanding of coronal heating requires that this be explained. V. Kashyap and R. Rosner (1994, unpublished results) attempted to study the birth of soft X-ray loops using SXT images, but a combination of data gaps and inadequate cadence prevented them from drawing any definitive conclusions. Litwin & Rosner (1993) pointed out that if loops turn on suddenly, the heating rate required to produce the hot plasma initially far exceeds the heating rate required to maintain its temperature in the presence of radiative and conductive losses. In other words, the heating profile describing how the heating rate varies with time must have a sharp spike followed by a lower level steady phase. Loops that turn on gradually, on the other hand, would indicate a heating rate that ramps up slowly to the maintenance level. Similarly, loops that fade rapidly (on the cooling timescale) indicate a heating that shuts off abruptly, and loops that fade gradually indicate a heating rate that diminishes slowly (see e.g., Serio et al. 1991, Jakimiec et al. 1992).

This view must be modified somewhat if loops are multi-stranded structures heated by many small nanoflares. In that case, a sudden loop brightening would mean that a flurry of nanoflares commences all at once, while a gradual turn on would indicate a steadily growing frequency of nanoflares. This last possibility could be related to the development of a self-organized critical system (López Fuentes et al. 2005; Klimchuk, López Fuentes, & DeVore 2006). In the context of such a picture, a gradual fading of the loop might indicate that criticality has been lost. Nanoflares would continue to occur, but with steadily diminishing frequency.

In this work, we analyze data from the Solar X-ray Imager (SXI) on board the Geosynchronous Operational Environmental Satellite 12 (GOES-12). This instrument has the advantage over SXT, used by PK95, that it can observe the solar corona continuously. Thus, despite having a lower spatial resolution, it is ideal for addressing the problems discussed above. Our primary objective is to study the long-term evolution of coronal loops and, thereby, to infer the time-dependent properties of the coronal heating mechanism. We study the complete life cycle of loops, including their birth, maintenance, and decay. We compute evolutionary timescales and cooling times, and compare them in order to test for quasi-static equilibrium. Due to the particular sensitivity of the SXI filters, the observed loops have phys-

ical properties (T and EM) that are intermediate between those of SXT and TRACE loops. We discuss how SXI loops fill a gap in a trend suggested by SXT and TRACE loops, which seems to support a picture of impulsive heating by nanoflares (Klimchuk 2004, 2006).

The paper is organized as follows. In Section 2, we describe the characteristics of SXI and the data used here. In Section 3, we present the analysis of the observed loops: we obtain light curves for the full loop evolution (Section 3.1), we compute T and EM (Section 3.2), and we calculate the radiative and conductive cooling times for the observed loops (Section 3.3). In Section 4 we discuss the implications of our results for coronal heating and derive a relationship between the observed light curves and the evolution of the heating for the quasi-static case, or the frequency of nanoflares for the impulsive heating case. These relationships can be used to test the validity of coronal heating models. We discuss our results and conclude in Section 5.

2. Description of the data

The SXI instrument was built by NASA's Marshall Space Flight Center with funding from the US Air Force (Hill et al. 2005, Pizzo et al. 2005). It is a broadband imager in the 6-60 Å bandpass that produces full-disk solar images with ~ 1 min cadence. The images consist of 512×512 pixel arrays with 5 arcsec resolution. The FWHM of the telescope point spread function is ~ 10 arcsec. A set of selectable thin-film entrance filters allows plasma temperature discrimination: Open, 3 polyimide (thin, medium and thick) and 3 beryllium (thin, medium and thick). Open and polyimide filters are sensitive to plasmas below 2 MK. Periods of orbital eclipse for GOES-12 are both widely spaced and brief (less than 2% of the total time); therefore, it is especially well suited for continuous tracking of coronal loops.

After scanning the SXI database in search of continuous observations of non-flaring ARs available in several filters, we selected data from 26–28 August, 2003. These observations were obtained before the hardware degradation suffered by SXI on 5 November, 2003, which affected its operation capabilities and possibly its spectral response (Hill et al. 2005). Figure 1 shows an image obtained at 00:10 UT on 28 August, 2003. Seven ARs were present on the solar disk during the selected dates. We created a movie of 457 coaligned images that were observed with the Open filter at a rate of 6 per hour. The images were rotated to have solar North up and shifted to a common disk center position using the SolarSoftware package and other programs that we developed.

3. Loop analysis

3.1. Loop evolution

Seven loops were selected from the movie for detailed study. They are shown in Figure 2 at the times of maximum intensity. These particular loops were chosen because they are relatively well isolated from other overlapping structures that could contaminate the measurements (for a discussion of the necessity of isolated loops, see e.g., Reale & Ciaravella 2006), and because there were no C-class or larger flares reported at the location of the loops.

To study the temporal evolution of the loops, we generated light curves using the following procedure. We first constructed sets of subimages that are corrected for differential rotation. This was necessary because most of the loops were observed for roughly half a day, while one could be followed for more than 24 hours. Since the corona is optically thin in soft X-rays, not all the emission along the line of sight comes from the structure we are interested in; thus, we substracted a background intensity from each of our loops. On a reference subimage of each loop set, we subjectively selected three areas, one covered by the loop and two by background regions on either side (see Fig. 3). We computed the average intensity of the pixels in each of these areas. We then subtracted the average background from the average loop intensity to obtain the intrinsic intensity of the loop. We repeated the process using the same loop and background areas for all the images of the set. Extreme care was taken in the subjective selection of the areas, so they always include only loop emission or only background emission for all of the images in the set. In no case did the actual loop drift out of the contour defined in the first image. Finally, we obtained light curves of the intrinsic intensity for each of the selected loops.

Loops are not uniformly bright, as can be seen in Figure 2 and as discussed by, for example, Reale & Ciaravella (2006) and Di Giorgio et al. (2003). We selected the brightest part of the loop to make the intrinsic intensity measurements (e.g., Fig. 3). In no case did the bright area appear to move during the lifetime of the loop. Propagating fronts have been observed in some TRACE loop studies, such as Reale et al. (2000), but there is no evidence of them in the analyzed SXI loops.

Figure 4 shows the light curves of all seven loops, plotted on a similar horizontal scale for easy comparison. Only part of the light curve of loop 2 is shown because it lived much longer than the others. The asterisks correspond to individual intensity measurements and the continuous lines are 5-point-running averages to highlight the overall evolution. It can be seen that the loops go through three rather distinct phases, which we define as the *rise*, main, and decay phases. We subjectively identify these phases by noting the times when there is a qualitative change in the slope of the smoothed light curve. The phases are marked

with thick straight lines in the panels of Figure 4. Table 1 lists the durations of the phases for all seven loops, together with the loop lifetime, which we define to span from the start of the rise phase to the end of the decay phase (i.e., the sum of the rise, main, and decay phase durations). The main phase of loop 7 is not clear, and it is possible that this loop evolves from a rise phase directly into a decay phase.

All of the light curves begin and end at a significant positive value of the intensity. This is somewhat surprising, since it is the intrinsic (background-subtracted) intensity that is plotted, and we might expect it to be closer to zero and even slightly negative in some cases. We offer two possible explanations. First, the plasma volume that we identify as the loop may have a low level of sustained heating that precedes the rise phase and continues beyond the decay phase. Second, the emission outside the loop volume may be brighter in the immediate vicinity of the loop, including just below it and above it, than in the more distant areas to the side that we have chosen to define the level of background emission.

The second possibility raises the issue of the uncertainty in the background subtraction and therefore the uncertainty in the intrinsic loop intensities we are trying to measure. We have assumed that the intensities to either side of the loop accurately characterize the background along the loop line of sight. One indication of the uncertainty in the background is the short-term variability in the side intensities. Table 1 lists for each loop the root-mean-square (rms) intensity variation of the side areas with respect to the 10-point running average. The values are given as a fraction of the intrinsic loop intensity averaged over the main phase. We consider these to be an estimate of the uncertainty in the intrinsic loop intensity. The average uncertainty for the seven cases is 6%. The table also lists the rms variation of the intrinsic intensity during the main phase relative to the main phase average. The mean value for all the loops is 7%, and we conclude that most of the measured variability is due to errors in the background subtraction. However, since our objective is to study the longer-term evolution of loops, the details of the short-term variability are not important. We note that the background evolves more slowly and with smaller amplitude than do the loops themselves.

Following PK95, we compute evolutionary timescales according to:

$$\tau_{evol} = \frac{I_m}{(\Delta I/\Delta t)},\tag{1}$$

where I_m is the mean intensity and $\Delta I/\Delta t$ is the mean intensity derivative for a given time interval, Δt . PK95 were only able to consider a single short (< 1 hr) interval for each loop, but we derive characteristic timescales for the full durations of the rise, main, and decay phases. They are based on the straight line segments drawn subjectively to match the actual light curve, as shown in thick lines in Figure 4.

The values of τ_{evol} for the three evolutionary phases are listed in Table 1. They are positive or negative depending on whether the intensity is increasing or decreasing, respectively. The durations of the phases are positive, by definition. The timescales and durations tend to be similar to each other for both the rise and decay phases. For the main phase, on the other hand, the timescales are 1–2 orders of magnitude longer than the durations. This is because the slope of the light curve is very small during the main phase. Many of the timescales measured by PK95 are very long (hundreds of hours), and it is likely that those loops were observed during their main phase. Note that the intensity can be either increasing or decreasing during the main phase. This may indicate that the energy input to the loop can be either very slowly increasing or very slowly decreasing during this time. However, we cannot rule out the possibility that imperfect background subtraction contributes to this result.

Litwin & Rosner (1993) argued that if loops are monolithic and turn-on suddenly, the onset time should be comparable to the sound-transit time (see also Fisher, Canfield, & McClymont 1984). For typical coronal loops the sound-transit time is of the order a few tens of seconds, which is much shorter than the typical rise phase timescales of our loops. We conclude that the loop-averaged heating must turn on slowly (though it could turn on quickly within the individual strands of a multi-stranded loop). As we will show in Section 3.3, the cooling times of our loops are much shorter than the decay phase timescales, so we also conclude that the loop-averaged heating turns off slowly. Considering the full evolution of the loops, it would seem that the heating must be of a similar nature in all three phases, including the main phase.

3.2. Loop temperatures and densities

In order to compute cooling times, for eventual comparison with the evolutionary timescales, we must first determine the temperatures and emission measures of the loops. As is customary with broadband instruments, T and EM are estimated using the filter ratio technique, which takes advantage of the fact that observations made with different wavelength bandpasses have different temperature sensitivities. The observed intensity is given by

$$I = \int n^2 S(T) \ dV = EM \ S(T) \tag{2}$$

for an isothermal plasma, where dV is the differential emitting volume, n is the electron density, and S(T) is the instrument response (for SXI see http://www.sec.noaa.gov/sxi/). For two different filters (a and b) with response functions $S_a(T)$ and $S_b(T)$, the ratio of the

intensities depends only on temperature:

$$R(T) = \frac{S_a(T)}{S_b(T)} = \frac{I_a}{I_b}.$$
(3)

Thus, from an observed filter ratio R(T) one can obtain an estimate of the temperature under the assumption that the plasma is isothermal. For a multi-thermal plasma, the inferred temperature will be a complicated weighted average, with greater weighting where the filters are more sensitive.

Since there are several possible filter combinations for T and EM diagnostics, we must decide which one is the most suitable for our observations. Figure 5 shows plots of R versus T for three different combinations: Open/thick-polyimide, Open/medium-polyimide and thick-polyimide/medium-polyimide. The Open/thick-polyimide combination has the steepest dependence on T in the range (≤ 2 MK) of maximum sensitivity of the filters. Therefore, we select that filter combination and compute the ratio of intrinsic loop intensities to obtain T using Equation 3. Once T is known, EM is obtained from Equation 2 using either of the two filters. Thick-polyimide images are taken approximately once every 7 hours. Since most of the studied loops live longer than that, we can compute at least one and sometimes two T values for each loop. The first value is from the main phase, and the second value, if available, is from near the end of the rise phase or near the beginning of the decay phase. The two T values turn out to be similar within error bars, and we average them to obtain a single temperature for the loop. The individual temperature values are themselves averages in that they are computed from spatially averaged loop intensities. The filter intensities in Equation 3 are obtained following the procedure described in Section 3.1.

Once we have estimates of T and EM, we can obtain the electron number density,

$$n = \left(\frac{EM}{fd}\right)^{1/2},\tag{4}$$

and the plasma pressure,

$$P = 2nkT, (5)$$

where f is the filling factor (the fraction of the observed volume occupied by emitting plasma), d is the loop diameter, and k is the Boltzmann constant. Here, we assume f = 1, so our density is a lower limit. We determine d following the procedure described in Klimchuk et al. (1992), PK95 and Klimchuk (2000), which is based on the calculation of the standard deviation (i.e., second moment) of the intensity profile (after background subtraction) in a direction perpendicular to the loop axis. It can be demonstrated that the standard deviation is $\frac{1}{4}$ of the loop diameter for well-resolved observations of uniformly filled loops having circular cross-sections. Actual loop observations suggest that the assumptions of a

circular cross-section and uniform density (on resolvable scales) are reasonable (see Klimchuk 2000, López Fuentes et al. 2006). Thus, for each loop we use the image of maximum loop brightness to compute the standard deviation of the intensity profile at every pixel position along the loop axis. We then obtain an average diameter for the loop that is four times the average of the standard deviations. Our measurements show that these values do not vary significantly along the loops (see also, Klimchuk 2000, López Fuentes et al. 2006).

The inferred temperatures and densities of the observed loops are shown in Table 1. The temperatures range between 1.2 and 2.3 MK, and the densities are of order 10⁹ cm⁻³. These loops are therefore cooler and more dense than most *Yohkoh*/SXT loops (PK95) and slightly hotter and less dense than most TRACE loops (Aschwanden et al. 1999, Aschwanden et al. 2001, Winebarger et al. 2003).

Our determinations of loop physical parameters have uncertainties that depend on the uncertainties in the intrinsic intensity measurements. The nominal error of SXI intensities, which is based on photon statistics and detector properties, is discussed by Pizzo et al. (2005). The uncertainty associated with N_{phot} detected photons is $\sqrt{2N_{phot}}$. We propagate these uncertainties through the T, EM, and n computations, taking full account of the fact that the T and EM uncertainties are not independent, but rather are correlated through the filter ratio R(T). See Klimchuk & Gary (1995) for a complete analysis of the errors associated with the filter ratio technique. We follow a similar approach here. The resulting uncertainties in T, EM, and n are typically 10% or less. We have not formally accounted for the uncertainties associated with the background subtraction, which depend primarily on our subjective choice of the background areas, but we have verified that the intrinsic loop intensities do not change significantly when the background areas are shifted by a few pixels in each direction.

3.3. Cooling timescales

The energy equation for coronal loops in quasi-static equilibrium describes a balance of thermal conduction, optically thin radiation, and an unknown mechanism of coronal heating, and is given by:

$$Q + \kappa_o \frac{d}{ds} \left(T^{5/2} \frac{dT}{ds} \right) - n^2 \Lambda(T) = 0, \tag{6}$$

where Q is the volumetric heating rate, s is the curvilinear coordinate along the loop, and we have neglected variations in the loop cross-sectional area. The second and third terms account for conductive and radiative losses, respectively. For those terms, $\kappa_o T^{5/2}$ is the thermal conductivity (with $\kappa_o = 10^{-6}$ erg s⁻¹ cm⁻¹ K^{-7/2}, Spitzer 1962), and $\Lambda(T)$ is the

optically thin radiation loss function.

An estimation of the cooling times can be obtained by dividing the energy density of the gas by the energy loss rate, L, associated with the corresponding process:

$$\tau \approx \frac{\frac{3}{2}P}{\mathbb{L}}.\tag{7}$$

If we are only interested in the gross properties of the loop, the conduction term can be approximated as:

$$\mathbb{L}_{cond} = \kappa_o \frac{d}{ds} \left(T^{5/2} \frac{dT}{ds} \right) \approx \frac{2}{7} \kappa_o \frac{T^{7/2}}{L^2}.$$
 (8)

where L is the loop half-length and T is the average loop temperature under the assumption that T is almost constant along most of the loop (see PK95 and references therein). Loop half-lengths have been estimated by visually identifying the locations of the footpoints in the straightened loop image used in the diameter measurement procedure. They are listed in Table 1. Substituting the above expression into Equation 7 gives the conductive cooling time:

$$\tau_{cond} \approx \frac{21}{4} \frac{k}{\kappa_o} \frac{PL^2}{T^{7/2}}.$$
 (9)

For the radiative cooling time, the radiative loss function $\Lambda(T)$ can be expressed as a power of T (Vesecky et al. 1979, Kano & Tsuneta 1995):

$$\Lambda(T) = \Lambda_o T^b, \tag{10}$$

where Λ_o and b are constants. Combining this with Equation 7 and the corresponding term in Equation 6 ($\mathbb{L}_{rad} = n^2 \Lambda(T)$), we obtain:

$$\tau_{rad} \approx \frac{6k}{\Lambda_o} \frac{T^{2-b}}{P}.\tag{11}$$

The constants Λ_o and b for the temperature range of the loops studied here are: $\Lambda_o = 1.9 \times 10^{-22}$ and b = 0 for $T \le 1.51$ MK, and $\Lambda_o = 3.53 \times 10^{-13}$ and b = -1.5 for T > 1.51 MK (PK95).

Finally, the net cooling time due to radiation and conduction acting together is given by:

$$\tau_{cool} = \left(\tau_{cond}^{-1} + \tau_{rad}^{-1}\right)^{-1}.\tag{12}$$

The computed τ_{cool} values are given in Table 1. The uncertainties, obtained by propagating the errors in the physical parameters, are of order 5%. Note that these cooling times correspond to the main phase, or very close to it. Using a simple analytical model, Serio et al.

(1991) obtained a slightly different expression for the cooling time that is approximately 0.7 times τ_{cool} given in Equation 12. This alternate form does not change the conclusions below.

We see from Table 1 that the evolutionary timescales of the three different phases are much longer than the cooling times: 4-15 times longer for the rise phase; 24-174 times longer for the main phase; and 2-13 times longer for the decay phase. In comparison, the evolutionary timescales of the loops studied by PK95 (although not stated in the paper) are between 2 and 9300 times longer than the cooling times, with a median value of 23. This suggests that most of the PK95 loops were observed during the main phase, as already noted. The table also shows that the durations of the evolutionary phases, including the main phase, are longer than the cooling times. These results indicate that the loops could be in quasi-static equilibrium.

Detailed solution of the hydrodynamic equations reveals that thermal conduction is a slightly stronger cooling mechanism than radiation in static equilibrium loops and therefore that $\tau_{rad}/\tau_{cond} \gtrsim 1$ (e.g., Vesecky et al. 1979). The last row in Table 1 gives the ratios computed for our loops. They are all less than, but not much less than, unity. This indicates that radiation is somewhat stronger than thermal conduction in these loops and, therefore, that they are not in quasi-static equilibrium. This can be reconciled with the result that the evolutionary timescales are much longer than the cooling times if we consider the loops to be bundles of unresolved impulsively-heated strands, as discussed below.

Figure 6 is a plot of the cooling time ratio, τ_{rad}/τ_{cond} , versus temperature. The seven SXI loops studied here are shown as diamonds, while the crosses come from measurements of Yohkoh/SXT loops at higher temperatures and TRACE loops at lower temperatures (Klimchuk 2006). The SXI values are intermediate between the SXT and TRACE values and help to define what appears to be a continuous diagonal band of points. There do *not* seem to be two physically distinct classes of loops.

It is interesting to speculate that the continuous distribution of loop properties indicated by Figure 6 implies that all loops are heated by the same mechanism, or that different mechanisms have fundamental similarities (e.g., are all impulsive or are all steady with similar rates of heating). If impulsive heating and steady heating were both common, we would expect Figure 6 to have a diagonal band of points from the impulsively heated loops (Klimchuk 2006) and a horizontal band of points at $\tau_{rad}/\tau_{cond} \gtrsim 1$ from the steadily heated loops. Furthermore, if there existed both strong and weak mechanisms of steady heating, we would expect a cluster of points at high temperature and a cluster of points at lower temperature, with few loops in between. Additional study of the frequency of different temperature loops is needed before anything definitive can be claimed.

4. Possible heating scenarios

As we have already mentioned in the Introduction, there are two basic scenarios for the heating of slowly evolving loops. In one case, loops are monolithic structures (or they are multi-stranded with all of the strands being identical), and the heat source changes slowly so that the plasma adjusts in a quasi-static fashion. In the other case, loops are bundles of impulsively heated strands, and the frequency of nanoflare events changes slowly. In this way the loop will appear to evolve gradually, even though the individual strands do not. A schematic representation of these two possibilities is shown in Figure 7 for the rise phase of a loop. In the upper panel, the intensity of the loop increases due to a slowly varying heat source that provides energy uniformly. The level of loop brightness, indicated by the hatching density, increases with time. In the lower panel, the number of elemental strands that are heated, i.e. the number of nanoflares, increases with time with each strand having the same brightness. It is possible to quantitatively relate the change in the loop intensity to either the change in the volumetric heating rate (monolithic loop) or the change in the nanoflare frequency (multi-stranded loop), as we now discuss.

4.1. Monolithic loops in quasi-static equilibrium

In quasi-static equilibrium, the three terms in the energy equation (Equation 6) are roughly equal (Vesecky et al. 1979):

$$Q \sim \frac{2}{7} \kappa_o \frac{T^{7/2}}{L^2} \sim n^2 \Lambda_o T^b. \tag{13}$$

From Equation 2, we know that the loop intensity is related to the instrument response function S(T) by:

$$I \propto n^2 S(T). \tag{14}$$

For the temperature range of the studied loops and the Open filter, the response function can be written as:

$$S(T) = S_o T^a, (15)$$

where S_o and a are constants, such that a = 0.93 for $T \le 1.51$ MK, and a = 0.54 for T > 1.51 MK. Combining the expression for S(T) with Equations 13 and 14, we obtain the following relationship between the volumetric heating rate and the loop intensity:

$$Q \propto I^{\phi},$$
 (16)

where the exponent ϕ is given by:

$$\phi = \frac{1}{1 + \frac{2}{7}(a - b)} = \begin{cases} 0.79 & 1MK \le T \le 1.51MK \\ 0.63 & 1.51MK < T \le 2.5MK. \end{cases}$$
 (17)

Therefore, the intensity profile (i.e., light curve) is a direct indication of the volumetric heating rate profile. The heating rate timescale, $\tau_Q = Q/(dQ/dt)$, and the intensity timescale, $\tau_I = I/(dI/dt)$, are then related in the following way:

$$\tau_Q = \phi^{-1} \tau_I. \tag{18}$$

The heating rate timescale is approximately 1.5 times longer than the intensity timescale.

It is important to bear in mind that the above analysis is valid only when the heating changes slowly enough that the physical conditions in the loop are close to static equilibrium. That is what is meant by quasi-static equilibrium. As a rule of thumb, quasi-static equilibrium applies whenever the heating rate timescale is several times longer than both the cooling timescale and the end-to-end sound transit timescale. These are the characteristic times required to achieve energy balance and force balance, respectively. As shown in Table 1, these conditions are met in our loops.

4.2. Multiple strands heated by nanoflares

Let us now consider loops that are bundles of impulsively heated elementary strands. We assume that the shape of the nanoflare energy distribution does not change during the lifetime of the loop, so that the ratio of large nanoflares to small nanoflares is the same at all times. We also assume that all strands cool completely before being reheated. Under those conditions, the average temperature of the heated strands will also not change. The intensity of the loop bundle is then a direct indication of the nanoflare occurrence rate:

$$I \propto \frac{dN}{dt},$$
 (19)

where dN is the number of nanoflares being produced at interval dt. Since the global heating rate of the loop (integrating over the strands) is proportional the rate of nanoflare occurrence, the timescale for the global heating rate will be equal to the intensity timescale:

$$\tau_Q = \tau_I. \tag{20}$$

Note that this relationship will not be accurate at the very start of the rise phase and very end of the decay phase, when the light curve will reflect the evolution of individual strands.

Equations 18 and 20 impose observational constrains on theories of coronal heating. Any complete theory must be able to explain the entire observed light curves of loops, including the different timescales during the rise, main, and decay phases.

5. Discussion and conclusions

The main aim of this work has been to investigate the long-term evolution of non-flaring coronal loops, from their initial brightening to their full decay. Soft X-ray observations taken by SXI, though having poorer spatial resolution than SXT and TRACE, have the advantage of extended and effectively continuous temporal coverage that allows us to undertake such a study without data gaps. Through a detailed analysis of seven loops observed from 26-28 August, 2003, we were able to verify and greatly broaden previous conclusions (PK95) that were based on short-term SXT observations.

We found that the temporal evolution of all our studied loops can be separated into three phases: rise, main and decay. The durations of the individual phases range from half an hour to as long as 7 hours. The total loop lifetimes range between about 4 hours and 1 day. The timescales that characterize the intensity variations range between roughly 3 and 16 hours for both the rise and decay phases and are 1-2 orders of magnitude longer for the main phase. An important result is that all of these timescales are considerably longer than the cooling time and sound-transit time (see Table 1).

We can draw the following conclusions from these results. First, the loop-averaged heating rate must increase slowly, reach a nearly constant level, and then decrease slowly. It is not the case that the heating turns on suddenly, which, as pointed out by Litwin & Rosner (1993), would imply that the heating has two dramatically different phases: an intense initial phase followed by a moderate maintenance phase. The fact that the heating changes slowly during all three evolutionary phases suggests that a single heating mechanism operates for the entire lifetime of the loop.

Considering that loops are formed by unresolved magnetic strands, the loop-averaged heating rate may be very different from the heating rate within individual strands. If the strands are all identical, so that the loop is a monolithic structure, then the local and global heating rates are the same. However, recent observational and theoretical evidence suggests that the strands are heated impulsively and are very different from each other at any instant in time (e.g., Klimchuk 2006 and references cited therein). In that case, the entire loop bundle may appear to evolve slowly even if the individual strands are evolving rapidly. The loop-averaged heating rate then reflects the frequency with which individual heating events

(nanoflares) are occurring, rather than the intrinsic variation of the heating rate within each strand. We have shown that the timescale of the loop-averaged heating rate is proportional to the timescale of the observed intensity variation under both scenarios. The constant of proportionality is approximately 1.5 for quasi-steady heating in monolithic loops and 1.0 for impulsive heating in multi-stranded loops.

Previous studies have shown that hot SXT loops $(T > 2 \times 10^6 \text{ K})$ are under dense compared to what is expected from quasi-static equilibrium solutions (PK95). On the other hand, warm TRACE (and SoHO/EIT) loops $(T \sim 10^6 \text{ K})$ are over dense (Aschwanden et al. 1999, Aschwanden et al. 2001, Winebarger et al. 2003). This is reflected in the ratio of the radiative to conductive cooling times shown in Figure 6, where SXI loops are identified with diamonds while the cluster of plus signs at higher temperatures correspond to SXT loops and those at lower ones to TRACE. Hot loops have a large ratio, indicating that thermal conduction dominates at low densities, while warm loops have small ratios, indicating that radiation dominates at high densities. Both results can be understood in terms of strands that are cooling after having been impulsively heated to high temperatures; SXT sees only the hot strands, and TRACE and EIT see only the warm strands.

SXI loops also fit naturally into this nonequilibrium picture. They are of intermediate temperature, and there is a correspondingly smaller imbalance between conduction and radiation. Radiation is modestly stronger than conduction in SXI loops, whereas conduction would be modestly stronger than radiation if they were in static equilibrium. The SXI loops begin to fill a gap between the SXT and TRACE points in Figure 6. They provide further evidence that all loops are physically related and may be heated by a common mechanism (e.g., Klimchuk 2006).

If loops are indeed bundles of impulsively heated strands, then we should observe SXT, SXI, and TRACE/EIT loops together at the same physical location. There will be a temporal shift, since it takes time for the plasma to cool from SXT to SXI to TRACE/EIT temperatures, but, depending on the duration of the "storm" of nanoflares, we may expect some overlap of the light curves detected by the different instruments (e.g., Winebarger & Warren 2005; Ugarte-Urra et al. 2006). Unfortunately, SXT and TRACE observations are not available for the loops in our study. The Yohkoh spacecraft was no longer operating, and TRACE was observing different active regions elsewhere on the solar disk. We do have a limited number of EIT observations in essentially the same 171 A band of TRACE. The cadence was very slow, so there are only one or two EIT images for each SXI loop. The visibility of the loops in the EIT images can be summarized as follows. Loops 1 and 4 can be seen during the decay phase, but not at the beginning of the main phase. Loop 5 can be seen at the end of the main phase. Loops 2, 3, and 6 can be seen during the rise phase,

but only as pairs of bright areas corresponding to the SXI footpoints. Loop 2 is also visible during the main phase, still as footpoint emission, but loop 3 is not. Loop 7 is short lived and does not coincide with any EIT images. Despite the better resolution, the EIT versions of the loops do not show significant differences in structuring or morphology with respect to their SXI counterparts, except of course in the cases where only footpoint emission is visible. Whether these multi-instrument observations are consistent with bundles of impulsively heated strands can only be answered with detailed modeling, which is beyond the scope of the present study.

Among the theoretical evidence of nanoflare heating is the demonstration that the secondary instability produces explosive energy release when the misalignment angle between adjacent magnetic flux tubes reaches a critical value (Dahlburg, Klimchuk, & Antiochos 2005). It is well known that the photospheric field is concentrated into elemental flux tubes of kG strength (e.g., Sánchez Almeida & Lites 2000). A single SXI loop must contain many hundreds to thousands of these tubes. Parker (1988) pointed out that the footpoints of the tubes are randomly displaced by turbulent convection, causing the field to become tangled in the corona. Magnetic energy is apparently released when the misalignment angle of the intertwined tubes reaches the secondary instability threshold.

This basic picture has many similarities to cellular automata models of self-organized critical (SOC) systems. We have recently begun to explore whether the observed SXI light curves can be explained by a simple SOC model (López Fuentes et al. 2005; Klimchuk, López Fuentes, & DeVore 2006). Our initial results are encouraging. We imagine that the coronal field is originally untangled. Photospheric convection shuffles the footpoints and progressively increases the tangling. In the early stages, relatively few pairs of adjacent tubes reach the secondary instability threshold, and the SXI intensity is relatively faint. As time proceeds, the emission brightens as the number of tube pairs reaching the threshold steadily increases. This is the rise phase. Eventually, a self-organized critical state is achieved in which the stressing of the field by convection is balanced by the destressing of the field by impulsive energy releases. This is the main phase, when the intensity is roughly constant. Finally, something causes the effectiveness of the footpoint shuffling to diminish, and the loop enters a decay phase when the critical state can no longer be maintained. The cause of this loss of effectiveness is not entirely clear. One possibility is that the concentration of kG tubes decreases as the tubes diffuse across the photosphere. Footpoint shuffling is efficient at tangling the field only when the random walk step size is longer than the characteristic footpoint separation. When this condition is not met, a random step will not necessarily wrap a flux tube around its neighbor and there is a reduced likelihood that the level of tangling will increase.

We are currently investigating the dependence of the predicted light curve on the various parameters of the model and plan to report the results in an upcoming paper. The observed SXI light curves described here provide important constraints, not only for this model, but all models of coronal heating.

We acknowledge the GOES/SXI team, in particular Vic Pizzo and James McTiernan for their helpful advise on the handling and interpretation of SXI data. We thank our referee Fabio Reale for his enriching suggestions and comments. C.H.M. thanks the members of the Solar-Terrestrial Relationships branch at NRL for their hospitality during her stay there. This work has been funded by NASA and the Office of Naval Research.

REFERENCES

Aschwanden, M. J., Newmark, J. S., Delaboudinière, J.-P., Neupert, W. M., Klimchuk, J. A., Gary, G. A., Portier-Fozzani, F., & Zucker, A. 1999, ApJ, 515, 842

Aschwanden, M. J., Schrijver, C. J., & Alexander, D. 2001, ApJ, 550, 1036

Cargill, P. J. 1994, ApJ, 422, 381

Cargill, P. J., & Klimchuk, J. A. 2004, ApJ, 605, 911

Dahlburg, R. B., Klimchuk, J. A., & Antiochos, S. K. 2005, ApJ, 622, 1191

Delaboudiniere, J.-P., et al. 1995, Sol. Phys., 162, 291

Di Giorgio, S., Reale, F., & Peres, G. 2003, A&A, 406, 323

Fisher, G. H., Canfield, R. C., & McClymont, A. N. 1984, ApJ, 281, L79

Handy, B. N., et al. 1999, Sol. Phys., 187, 229

Hill, S. M., et al. 2005, Sol. Phys., 226, 255

Jakimiec, J., Sylwester, B., Sylwester, J., Serio, S., Peres, G., & Reale, F. 1992, A&A, 253, 269

Kano, R., & Tsuneta, S. 1995, ApJ, 454, 934

Klimchuk, J. A. 2000, Sol. Phys., 193, 53

Klimchuk, J. A. 2002, in G. Fisher and D. Longcope (eds.), ITP Conf. on Solar Magnetism and Related Astrophysics, U. California Santa Barbara (http://online.kitp.ucsb.edu/online/solar_c02/klimchuk/).

Klimchuk, J. A. 2004, in Proceedings of the SOHO 15 Workshop: Coronal Heating (ESA SP-575), ed. J. Ireland & R. Walsh (Noordwijk: ESA/ESTEC), 2

Klimchuk, J. A. 2006, Sol. Phys., 234, 41

Klimchuk, J. A., & Gary, D. E. 1995, ApJ, 448, 925

Klimchuk, J. A., Lemen, J. R., Feldman, U., Tsuneta, S., & Uchida, Y. 1992, PASJ, 44, L181

Klimchuk, J. A., López Fuentes, M. C., & DeVore, C. R. 2006, in Proceedings of SOHO-17: Ten Years of SOHO and Beyond (ESA SP-617), ed. H. Lacoste (Noordwijk: ESA/ESTEC)

Litwin, C., & Rosner, R. 1993, ApJ, 412, 375

López Fuentes, M. C., Klimchuk, J. A. & Démoulin, P. 2006, ApJ, 639, 459

López Fuentes, M. C., Klimchuk, J. A., & Mandrini, C. H. 2005, Eos. Trans. AGU, 86(18), Jt. Assem. Suppl., Abstract SP14A-06

Orrall, F. Q. 1981, Solar Active Regions: A monograph from Skylab Solar Workshop III

Parker, E. N. 1988, ApJ, 330, 474

Pizzo, V. J., et al. 2005, Sol. Phys., 226, 283

Porter, L. J. & Klimchuk, J. A. 1995, ApJ, 454, 499

Reale, F., Peres, G., Serio, S., DeLuca, E. E., & Golub, L. 2000, ApJ, 535, 412

Reale, F., & Ciaravella, A. 2006, A&A, 449, 1177

Rosner, R., Tucker, W. H., & Vaiana, G. S. 1978, ApJ, 220, 643

Sánchez Almeida, J., & Lites, B. W. 2000, ApJ, 532, 1215

Serio, S., Reale, F., Jakimiec, J., Sylwester, B., & Sylwester, J. 1991, A&A, 241, 197

Spitzer, L. 1962, Physics of Fully Ionized Gases (Interscience, New York), p.144

Tsuneta, S., et al. 1991, Sol. Phys., 136, 37

Ugarte-Urra, I., Winebarger, A. R., & Warren, H. P. 2006, ApJ, 643, 1245

Vesecky, J. F., Antiochos, S. K., & Underwood, J. H. 1979, ApJ, 233, 987

Warren, H. P., Winebarger, A. R., & Mariska, J. T. 2003, ApJ, 593, 1174

Winebarger, A. R., & Warren, H. P. 2005, ApJ, 626, 543

Winebarger, A. R., Warren, H. P., & Mariska, J. T. 2003, ApJ, 587, 439

This preprint was prepared with the AAS LATEX macros v5.2.

Table 1: Properties of the studied loops. All time values are given in hours. Loop and background rms are relative to the averaged loop intrinsic intensity during the main phase.

	Loop 1	Loop 2	Loop 3	Loop 4	Loop 5	Loop 6	Loop 7
Date	8/27	8/27	8/27	8/27	8/28	8/28	8/28
Start time (UT)	16:00	21:20	21:10	9:40	1:40	11:30	12:30
Temperature (MK)	1.5	1.6	1.7	1.8	1.2	1.9	2.1
Density $(10^9 cm^{-3})$	0.9	1.3	1.1	0.9	1.1	1.2	1.9
Loop length $(10^9 cm)$	11	5.8	12	7.2	9.1	5.4	6.5
Lifetime	10.9	> 27.4	15.2	11.6	10.9	6.4	4.2
Rise duration	3.2	5.2	6.2	3.6	3.6	3.2	2.2
Rise timescale	3.6	8.5	7.8	5.7	4.7	3.4	2.2
Main duration	4.7		4.2	3.1	2.9	1.4	0.5
Main timescale	21.3		-83.0	132.2	16.7	-48.1	-31.4
Decay duration	3.0		4.9	4.9	4.4	1.8	1.5
Decay timescale	-2.0		-8.5	-4.5	-7.6	-9.7	-1.7
Loop rms	0.08	0.04	0.03	0.08	0.06	0.06	0.13
Background rms	0.05	0.04	0.04	0.08	0.04	0.02	0.12
Cooling timescale	0.89	0.57	0.85	0.76	0.64	0.57	0.53
$ au_{rad}/ au_{cond}$	0.33	0.24	0.11	0.50	0.06	0.71	0.26
Sound-transit time	0.013	0.013	0.011	0.014	0.013	0.02	0.028

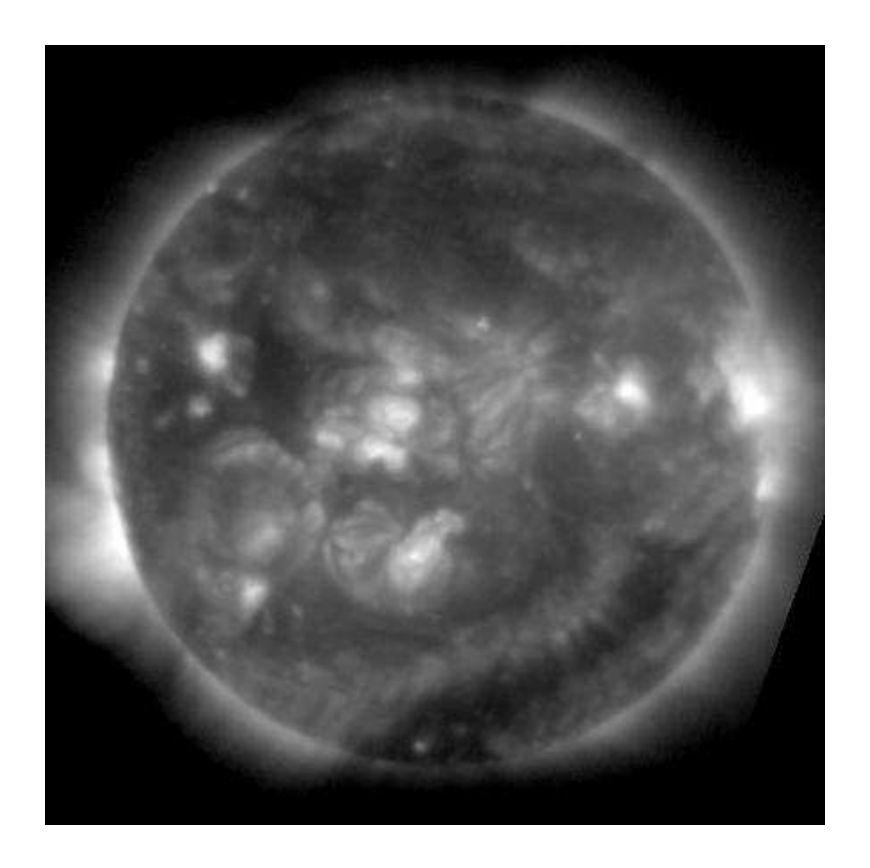


Fig. 1.— GOES-SXI image of the solar disk obtained with the Open filter at 00:10 UT on 28 August, 2003. Some of the studied loops can be seen in this image (see Fig. 2).

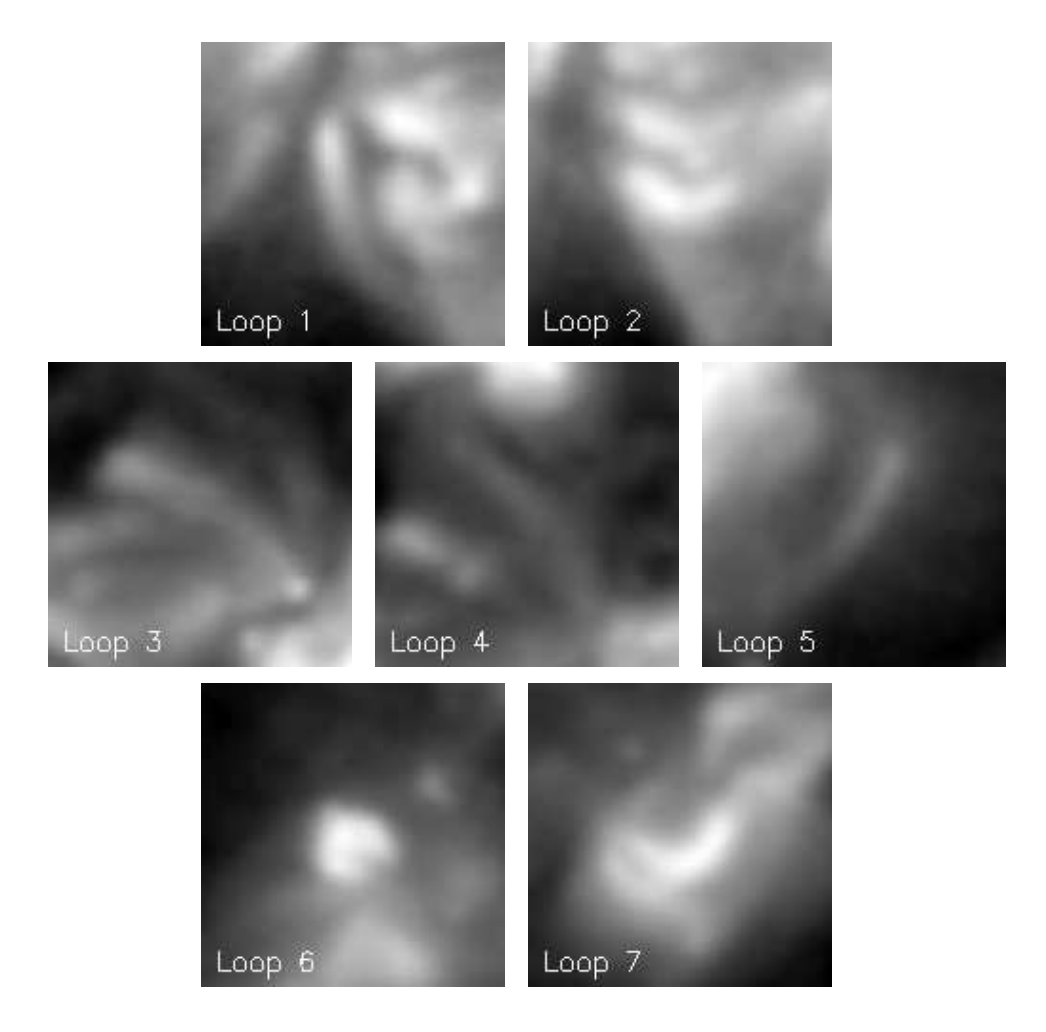


Fig. 2.— Closeup Open filter images of the SXI loops used in the study. On each image the corresponding loop is located at the center of the frame. The images correspond to the times of maximum loop intensity (during the main phase of their evolution, see Section 3.1) and display a square field of view having 100 Mm side.

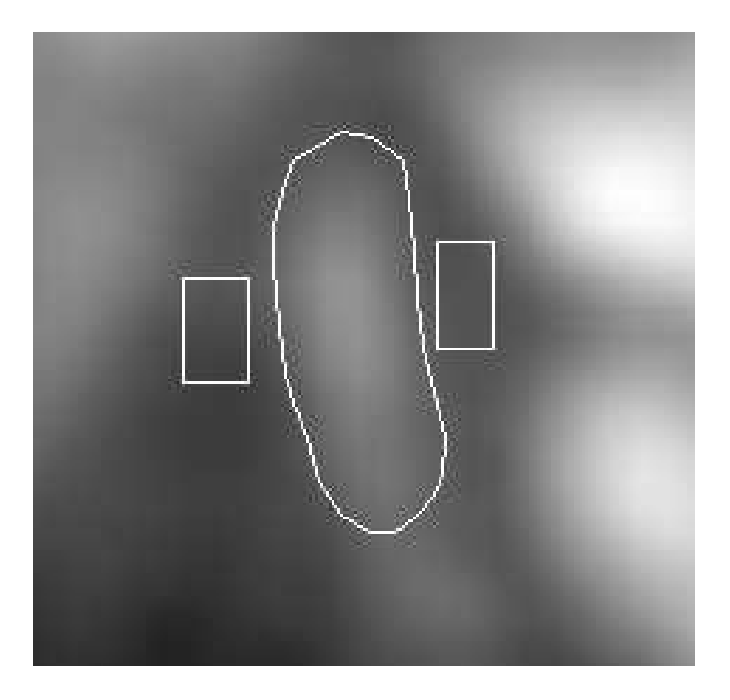


Fig. 3.— Regions used to determine the loop and background intensities for Loop 1 (see Figure 2). The average intensity per pixel from the square background regions is subtracted from the loop region to obtain the intrinsic loop intensity.

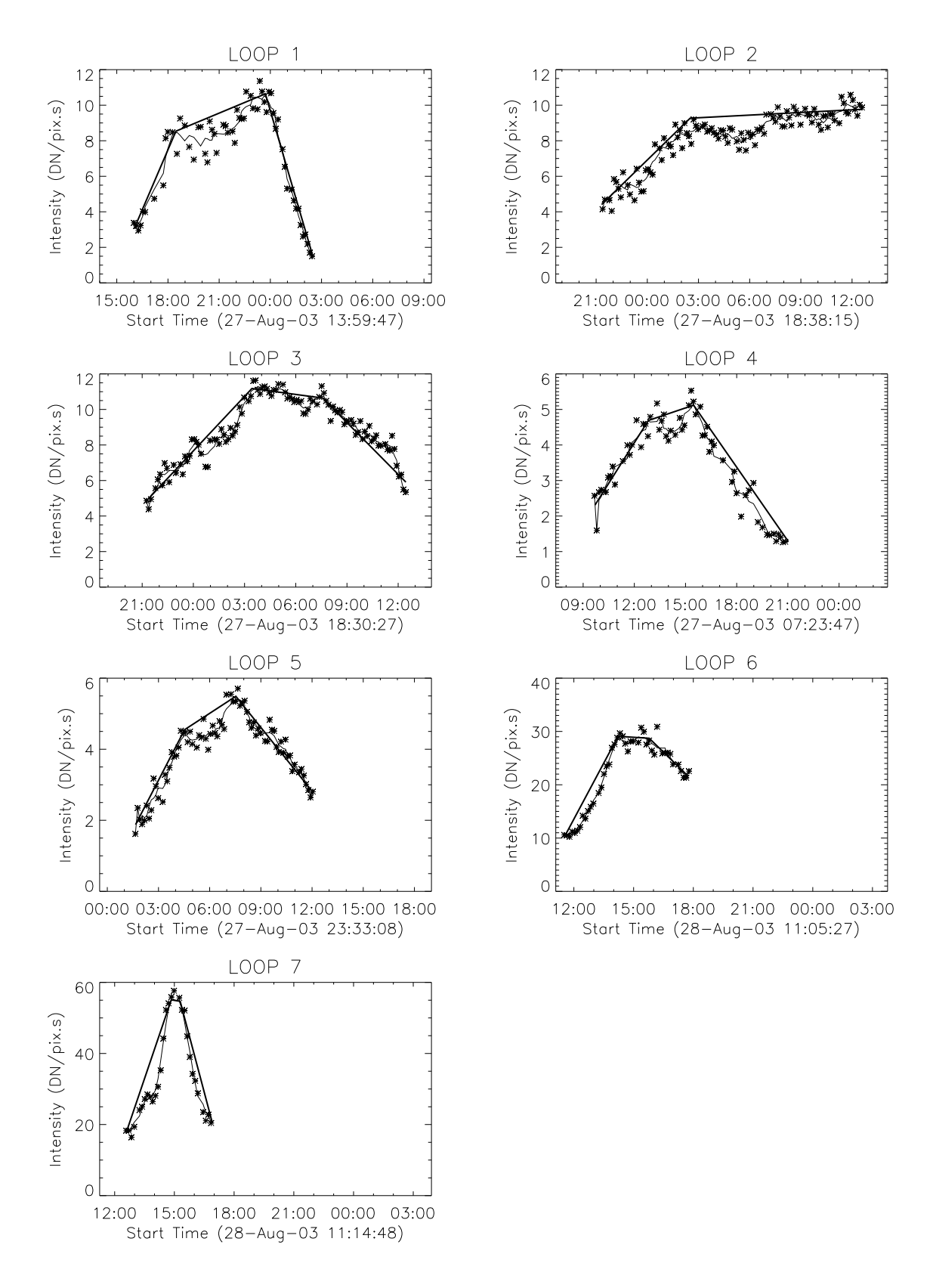


Fig. 4.— Lightcurves of all the observed loops constructed from the intrinsic (background subtracted) intensities obtained from sets of coaligned images. Asterisks correspond to individual measurements (one per image); the solid line is a 5 point-running average; and the thick straight lines mark the subjectively identified rise, main, and decay phases of the evolution (see Section 3.1).

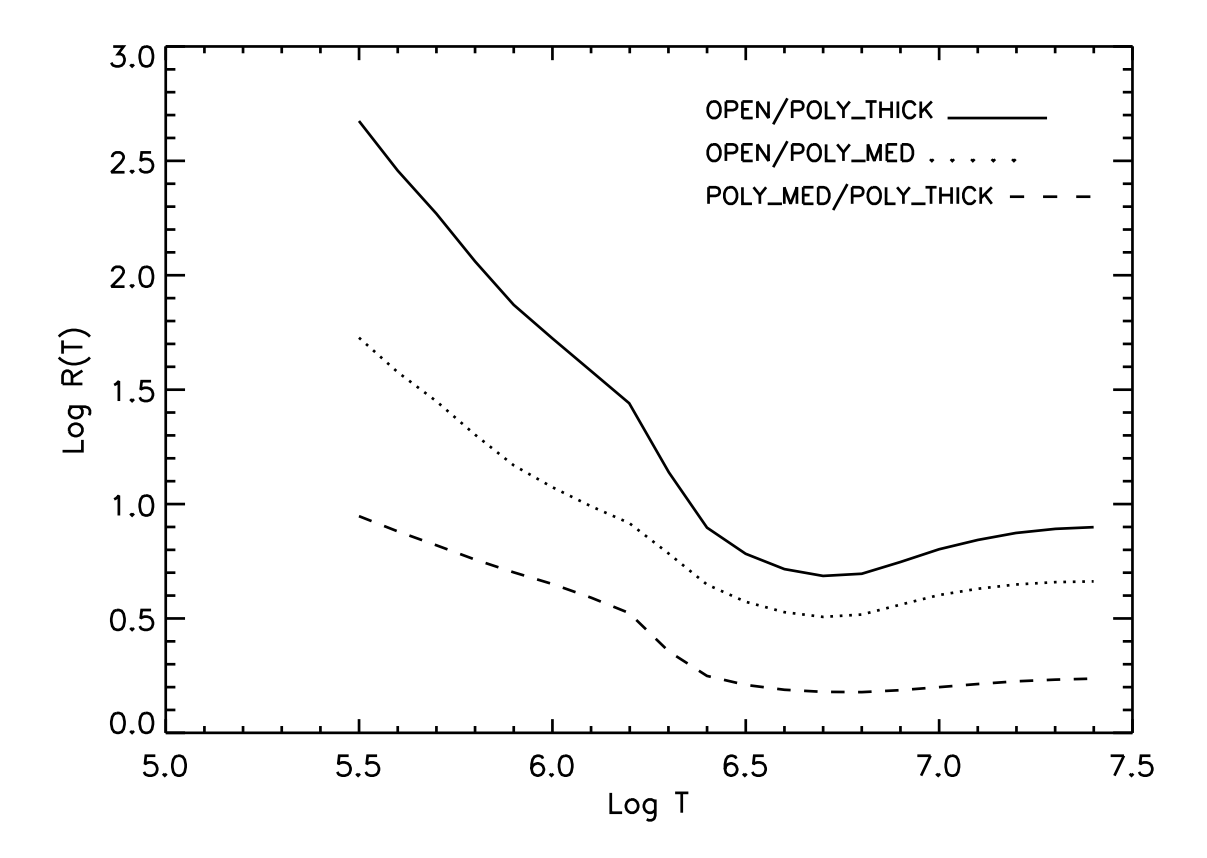


Fig. 5.— Filter ratio versus temperature for three different filter combinations. Open/thick-polyimide is the most suitable combination for our purposes since it has the steepest dependence on T in the range of maximum sensitivity of the filters (T < 2 MK).

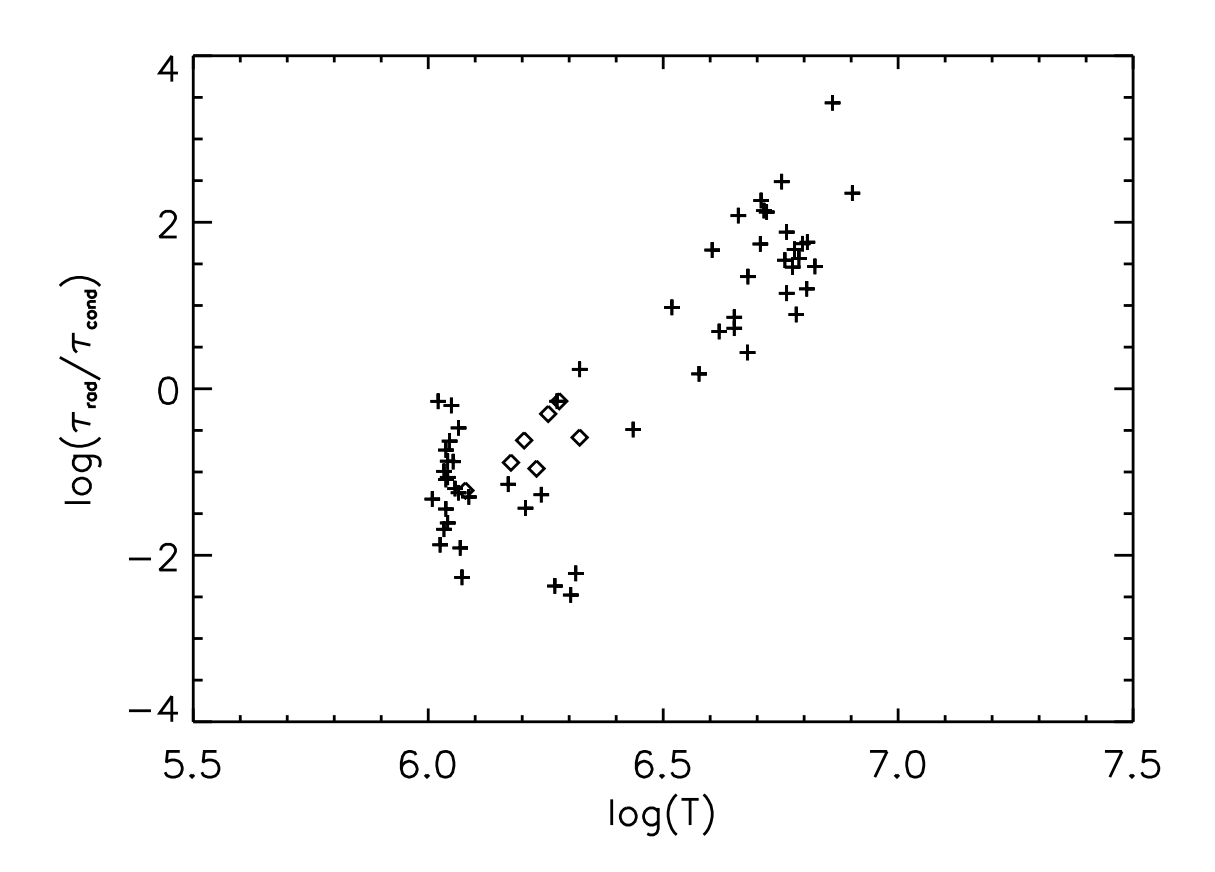


Fig. 6.— Ratio of radiative to conductive cooling times versus loop temperature. Pluses correspond to *Yohkoh*/SXT and TRACE loops, while diamonds correspond to the SXI loops studied here. Adapted from Klimchuk (2006).

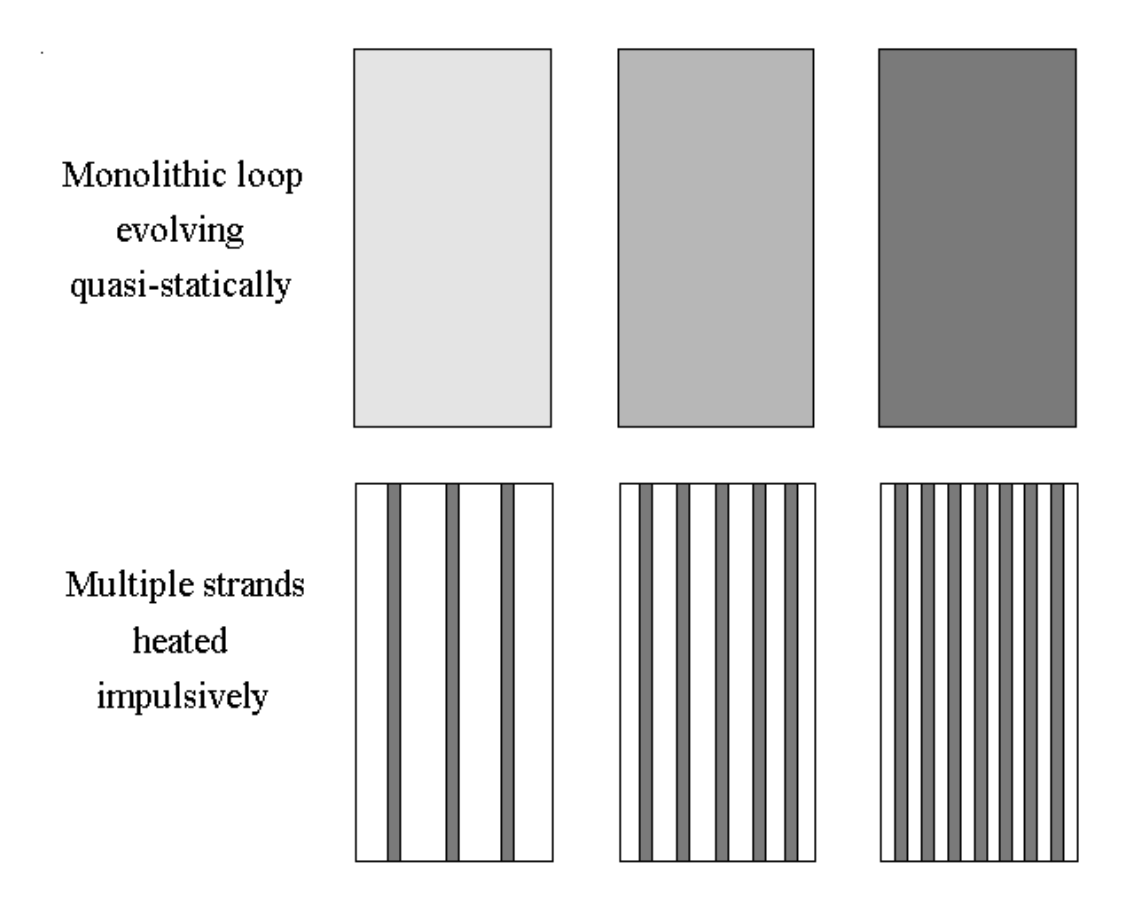


Fig. 7.— Sketch of the rise phase of a loop according to the two different heating scenarios discussed in Section 4. The upper panel corresponds to a monolithic loop that evolves quasi-statically as the heat source slowly and uniformly provides energy. The lower panel shows a loop comprised of many unresolved strands that are heated impulsively. The intensity increases with the number of heated strands (i.e., the nanoflare occurrence rate).